

# Supporting information for:

## Linking morphology and performance of organic solar cells based on decacyclene triimide acceptors

Gregory M. Su,<sup>†</sup> Toan V. Pho,<sup>‡</sup> Nancy D. Eisenmenger,<sup>†</sup> Cheng Wang,<sup>¶</sup> Fred Wudl,<sup>‡</sup> Edward J. Kramer,<sup>†,§</sup> and Michael L. Chabinyc<sup>\*,†</sup>

*Materials Department, University of California, Santa Barbara, California, 93106, United States, Department of Chemistry, University of California, Santa Barbara, California, 93106, United States, Advanced Light Source, Lawrence Berkeley National Laboratory, Berkeley, California 94720, United States, and Department of Chemical Engineering, University of California, Santa Barbara, California, 93106, United States*

E-mail: mchabinyc@engineering.ucsb.edu

## Experimental

### Fabrication of photovoltaic devices

Poly(3-hexylthiophene) (P3HT) was obtained from Rieke Metals (Sepiolid P200). DTI was synthesized as reported by Pho et al.<sup>S1</sup> Pre-patterned ITO-coated glass substrates were cleaned by sonicating inalconox:water, water, acetone, and isopropanol sequentially for 20 mins each. The

---

\*To whom correspondence should be addressed

<sup>†</sup>Materials Department

<sup>‡</sup>Department of Chemistry

<sup>¶</sup>Advanced Light Source

<sup>§</sup>Department of Chemical Engineering

substrates were dried with a stream of N<sub>2</sub> and exposed to oxygen plasma for ~5 mins. PEDOT:PSS (Clevios PVP Al 4083) was spin coated at 4000 rpm for 45 s onto the cleaned glass/ITO substrates, and dried at 160 °C for 20 min. The P3HT:DTI solutions (1:1 by weight) were prepared with a total concentration of 20 mg mL<sup>-1</sup> in o-dichlorobenzene with 1-chloronaphthalene (2% by volume) and stirred at 80 °C overnight. The P3HT:DTI solution was filtered (0.45 μm PTFE filter) directly onto the substrate in a N<sub>2</sub> filled glove box, and the substrate was spun at 1000 rpm for 60 s and then 2000 rpm for 10 s, yielding an active layer thickness of ~100 nm. The wet films were allowed to dry at room temperature for 20 mins. A 1 nm thick layer of LiF followed by ~90nm of Al was thermally evaporated on top of the active layer under vacuum (<10<sup>-6</sup> torr). The active area of the devices was 0.06 cm<sup>2</sup>, and current-voltage (J-V) characteristics were measured at 1 sun (AM 1.5G) in a N<sub>2</sub> filled glove box with a Xenon lamp (Newport) and a Keithley 2408 Source Measure Unit (SMU).

Electron-only diodes were fabricated in a similar way as the OPV devices. ITO-coated glass substrates were cleaned in the same way, but instead of PEDOT:PSS, a 90 nm layer of Al was thermally evaporated onto the glass/ITO substrates, followed by spin casting of the P3HT:DTI active layer. Finally, a 25 nm layer of Ca and a 90 nm layer of Al were evaporated on top of the active layer. Current-voltage measurements were performed in the dark. Hole-only diodes were fabricated similarly to the OPV devices, except a 90 nm layer of Au was evaporated onto the active layer instead of LiF/Al.

## **Differential scanning calorimetry (DSC)**

DSC measurements were carried out on a TA Instruments DSC 2920 differential scanning calorimeter. About 4 mg of material was loaded into a Tzero aluminum pan. Each samples was first equilibrated at 25 °C, then heated to 270 °C, cooled to 0 °C, and heated again to 270 °C. All of the heating and cooling cycles were done at a rate of 10 °C/min. An empty Tzero pan was used as a reference.

## **Grazing incidence wide angle X-ray scattering (GIWAXS)**

Samples were prepared for GIWAXS by spin-coating solutions of DTI or P3HT:DTI blends onto PEDOT:PSS coated Si substrates using the same deposition conditions as for the photovoltaic devices. GIWAXS experiments were performed at the Stanford Synchrotron Radiation Lightsource (SSRL) at beamline 11-3. A MAR 2300 area detector was used for 2D diffraction pattern collection. The energy of the incident beam is 12.7 keV. The angle of incidence used was  $0.11^\circ$  and the sample-to-detector distance was 40 cm. Samples were kept in a helium atmosphere to minimize X-ray damage and background scattering. Exposure times were typically between 30 s and 120 s. Beamline 11-3 is equipped with a heating stage that allows for GIWAXS scans to be taken at temperature for *in situ* studies.

## **Near edge X-ray absorption fine structure (NEXAFS)**

Samples for NEXAFS were prepared by spin-coating onto Si/PEDOT:PSS substrates, just as for GIWAXS. NEXAFS experiments were performed at beamline U7A at the National Synchrotron Light Source (NSLS). The incident X-ray beam was elliptically polarized (polarization factor = 0.85) with the electric field vector predominantly in the plane of the storage ring. The incident angle,  $\theta$ , was varied between  $30^\circ$  and  $90^\circ$ , where  $90^\circ$  refers to an incident X-ray beam that is perpendicular to the substrate. A spherical grating monochromator was used to select soft X-rays in the range from 280 eV to 440 eV, corresponding to the carbon and nitrogen K edges. The partial electron yield (PEY) data was collected with a channeltron electron multiplier with an adjustable entrance grid bias that was set to -150 V. All experiments were done in a UHV chamber. Carbon edge PEY and fluorescence yield (FY) data were normalized by subtracting a linear pre-edge baseline and setting the edge jump to unity at 325 eV.

## **Resonant soft X-ray scattering (RSoXS)**

RSoXS was performed at beamline 11.0.1.2 at the Advanced Light Source (ALS). Samples were prepared by spin coating P3HT:DTI blends onto Si/SiO<sub>2</sub>/PEDOT:PSS substrates, using the same conditions as for devices, and then floating onto 1.5 mm x 1.5 mm, 100 nm thick Si<sub>3</sub>N<sub>4</sub> membranes supported by a 5 mm x 5 mm Si frame (Norcada Inc.). 2D scattering was collected in a transmission geometry with a sample-to-detector distance of 160 mm. Data was collected on an in-vacuum CCD camera (Princeton Instrument PI-MTE) cooled to -45 °C. 2D scattering data was then reduced by azimuthal averaging of the scattering data over all  $q$  values. The RSoXS profiles shown in the manuscript were taken at 284.4 eV, an energy where there is a significant absorption difference between P3HT and DTI. Details of the specifics of this beamline have been reported elsewhere.<sup>S2</sup>

## **Dynamic secondary ion mass spectrometry**

Experiments were performed on a Physical Electronics 6650 Quadropole dynamic SIMS. A 2 kV O<sup>2+</sup> primary ion beam at ~45 nA was used and rastered over a 200 μm × 200 μm area and secondary ions were only collected from the middle 15% of this area. Si/SiO<sub>2</sub> substrates were used with a final sample geometry of Si/SiO<sub>2</sub>/PEDOT:PSS/P3HT:DTI/PS.

## Molecular geometry of DTI

Similar to decacyclene, DTI is found to have a gently twisted propeller geometry, as shown in Figure S1. Considering this, it is reasonable to expect DTI molecules to stack one on top of the other. However, adjacent molecules may need to twist to reduce steric interactions.

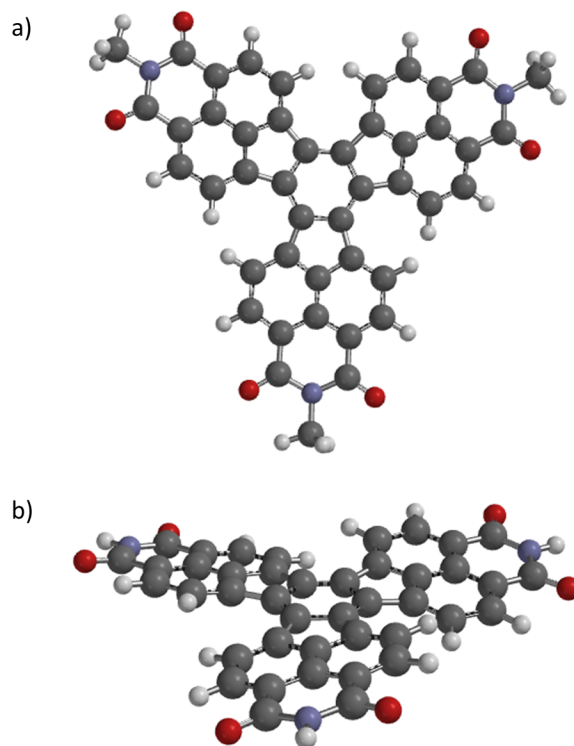


Figure S1: Molecular geometry of DTI calculated with DFT using the B3LYP/6-31G\* level of theory. The octyl side chains were replaced by methyl groups. A top-down view is shown in (a), and a side-view in (b).

## Effect of annealing on device performance

As discussed in the manuscript, thermal annealing leads to significant decreases in power conversion efficiency (PCE) of P3HT:DTI devices when annealed at 120 °C for 20 minutes, as shown in Figure 1. Furthermore, devices annealed at lower temperatures also exhibited diminished PCEs. For devices fabricated with a geometry of ITO/PEDOT:PSS/P3HT:DTI/Al (which has an overall

lower efficiency), PCEs of 0.37%, 0.05%, and 0.03% were measured for annealing temperatures of 50 °C, 80 °C, and 120 °C, respectively (Figure S2)

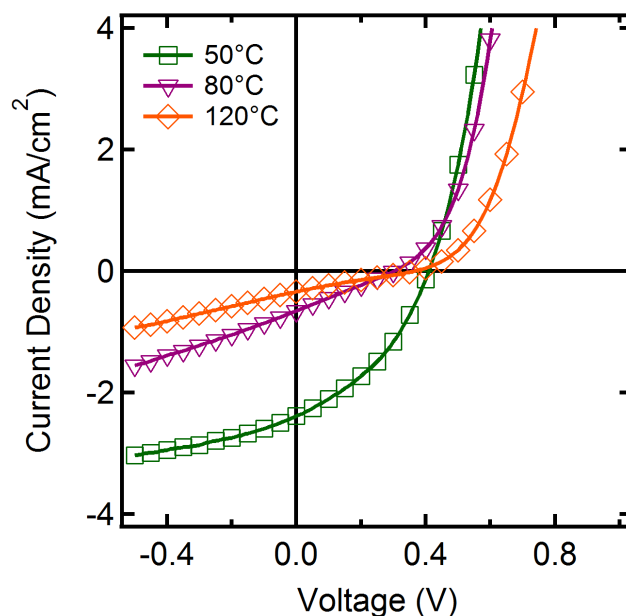


Figure S2: Current density vs. voltage curves for P3HT:DTI solar cells annealed at 50 °C (green squares), 80 °C (purple triangles), and 120 °C (orange diamonds).

## Surface topography with atomic force microscopy

AFM experiments were performed on an Asylum Research MFP 3D AFM using NanoWorld Point-probe Al-coated noncontact mode Si cantilevers with a spring constant of 48 N/m and a resonant frequency of 190 kHz. Surface topography of pristine DTI films and P3HT:DTI blends were investigated. Height images are shown in Figure S3. Large crystals are evident after thermal annealing of pristine DTI. However, blend films show relatively little difference in height topography beyond a slight increase in rms roughness from ~2.1 nm to ~2.8 nm for as-cast and annealed blends, respectively.

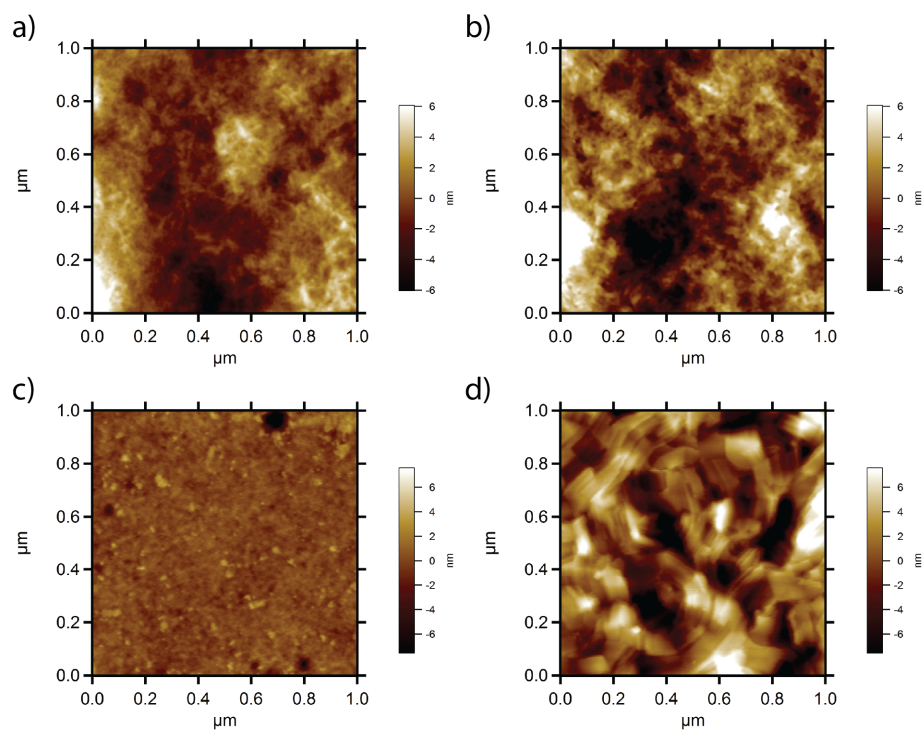


Figure S3: AFM height images of (a) an as-cast P3HT:DTI blend film, (b) an annealed (120 °C) P3HT:DTI blend film, (c) an as-cast pristine DTI film, and (d) an annealed pristine DTI film.

## Photoluminescence quenching

Photoluminescence (PL) quenching is commonly used to estimate the degree of charge transfer between materials in a blend upon photoexcitation. PL (Horiba FluoroMax-4 Spectrofluorometer) of as-cast and annealed P3HT:DTI blends excited at 430 nm (where absorption is dominated by DTI) and 570 nm (absorption dominated by P3HT) is shown in Figure S5.

It is clear that the PL intensity is much less in the annealed film excited at 430 nm, suggesting improved charge transfer from DTI to P3HT upon annealing. Based on the PL spectra of the blend films and pristine P3HT and DTI, it is estimated that the PL from DTI is 76% and 90% quenched for the as-cast and annealed P3HT:DTI blends, respectively. Although DTI crystallite size increases with annealing, enhanced charge transfer from DTI to P3HT is suggested from the increased PL quenching. This could be due to a large exciton diffusion length along the column direction of ordered columnar liquid crystals (up to about 60 nm),<sup>S3</sup> or energy transfer from DTI to P3HT. The PL quenching of P3HT (excited at 570 nm) did not change significantly, decreasing

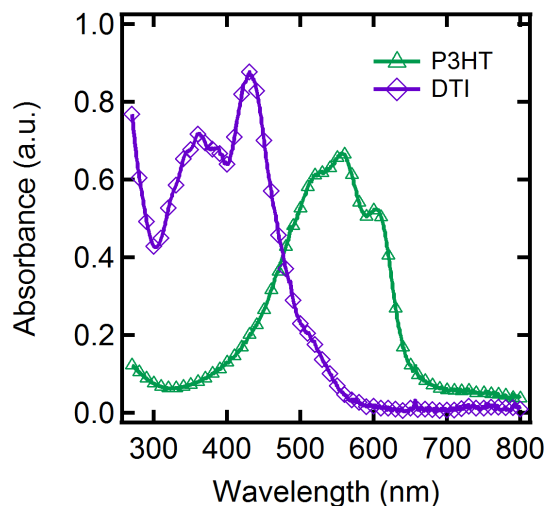


Figure S4: UV-Vis absorption of DTI and P3HT thin films.

from 60% P3HT quenching in the as-cast blend film to 53% in the annealed film. It is not surprising that charge transfer from P3HT to DTI is marginally reduced with annealing since P3HT domains become slightly larger (see Figure S18).

A higher degree of PL quenching is typically linked to improved solar cell performance due to enhanced charge transfer. However, the annealed P3HT:DTI solar cells have much lower efficiencies. This suggests that annealing does not reduce charge transfer and separation between P3HT and DTI, but rather these separated charges cannot be extracted to the contacts due to morphological aspects including molecular orientation and domain separation.

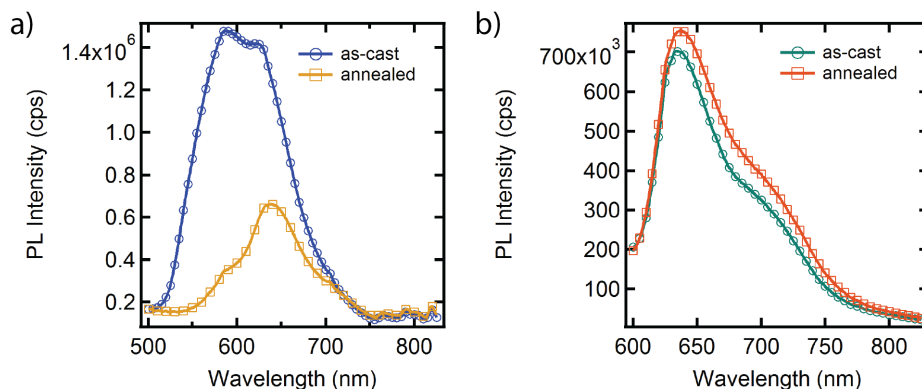


Figure S5: Photoluminescence spectra of as-cast and annealed P3HT:DTI thin films excited at (a) 430 nm and (b) 570 nm.

## Near edge X-ray absorption fine structure (NEXAFS)

### Carbon K edge spectra for P3HT and DTI

Organic semiconductors, which contain mainly carbon atoms and have many double bonds, exhibit rich spectra around the carbon K edge. The PEY spectra around the carbon K edge for pristine DTI and pristine P3HT is shown in Figure S6. Clear transitions from core electrons to  $\pi^*$  antibonding orbitals are visible as peaks near 285 eV. Higher energy peaks correspond to transitions to  $\sigma^*$  antibonding orbitals.

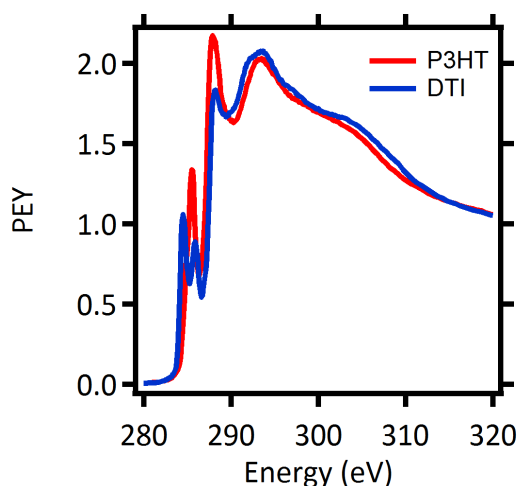


Figure S6: PEY NEXAFS spectra for P3HT (red curve) and DTI (blue curve) at energies near the carbon K edge. The incident angle was  $55^\circ$ .

### Surface composition

An estimate of the surface composition of the P3HT:DTI blends can be determined by fitting the NEXAFS spectra of the blend film with a linear combination of the spectra from individual components. Estimates on surface composition are shown in Figure S7. There is no drastic change in surface composition between as-cast and annealed blends, considering that the  $\pi^*$  peak of P3HT overlaps with one of the  $\pi^*$  peaks of DTI, which can complicate the fitting. Nevertheless, the result suggests the possibility that there is a slight excess of P3HT on the surface of the as-cast film, and the relative amount of P3HT on the surface decreases with annealing, as indicated in the DSIMS.

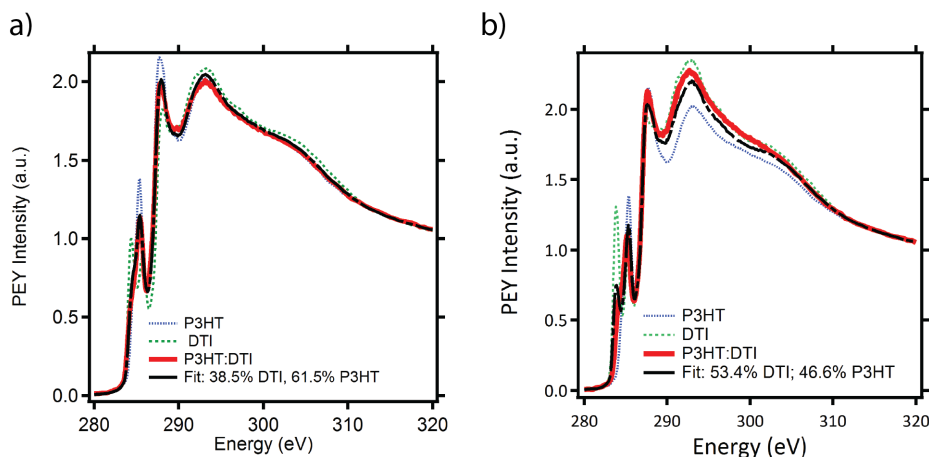


Figure S7: Surface composition fits for (a) an as-cast P3HT:DTI blend and (b) an annealed (120 °C) P3HT:DTI blend. Fits are based on a linear combination of the spectra of pure components. The incident angle was 60°.

## Probing molecular orientation with NEXAFS

NEXAFS experiments can probe molecular orientation due to the inherent polarization of the X-ray beam and the tunability of the incident angle. Organics often have anisotropic molecular orbitals and transitions to these orbitals can have dipole moments in a specific direction.<sup>S4,S5</sup> A  $\pi^*$  transition can typically be described by a vector that is perpendicular to the conjugated ring plane. The intensity of this peak will be greatest when the electric field vector of the X-ray is aligned with the direction of the  $\pi^*$  transition vector, and lowest when these two vectors are perpendicular, as depicted schematically in Figure S8.

Overall molecular orientation can be probed by changing the incident angle and tracking the total intensity of a specific transition. For different angles of the X-ray relative to the substrate plane,  $\theta$ , the PEY intensity of an X-Y bond is expected to vary linearly with  $\sin^2(\theta)$ , as given by,

$$I_{XY}(\theta) = a_{XY} + b_{XY}\sin^2(\theta).$$

Hence, molecular orientation can be quantified by plotting the total intensity vs.  $\sin^2(\theta)$ . Based

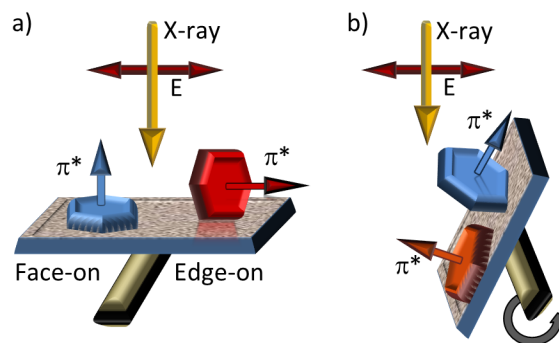


Figure S8: Schematic depicting the effect of incident angle on the intensity of a specific transition. Molecules that have a well defined transition dipole vector (in this case a  $\pi^*$  transition) will have the greatest intensity of that transition at an angle when it is in-line with the electric field vector,  $E$ . Here, we see that an edge-on molecule with a  $\pi^*$  transition parallel to the substrate surface will have a high  $\pi^*$  transition intensity when (a) the incident X-ray is perpendicular to the substrate ( $\theta = 90^\circ$ ) and lower when (b) the incident beam is more parallel to the substrate. The opposite would be true for a face-on molecule.

on a linear fit to this data, an orientation order parameter,  $S$ , can be determined as follows,<sup>S6</sup>

$$S = -\frac{P^{-1}b_{xy}}{3a_{xy} + (3 - P^{-1})b_{xy}},$$

where  $P$  is the polarization factor of the X-ray beam, in this case 0.85.  $S$  ranges from +1 for a transition dipole moment along the surface normal (face-on for a  $\pi^*$  transition) to -1/2 for a transition dipole moment in the plane of the substrate (edge-on for a  $\pi^*$  transition). Since  $S$  is based on the linear best fit, it is important to have at least a few angles between  $0^\circ$  and  $90^\circ$ . An example of this type of analysis for as-cast and annealed ( $120^\circ\text{C}$ ) DTI films is shown in Figure S9. It is clear that the annealed DTI film has an overall much more edge-on orientation with its orientation order parameter of  $S = -0.33$  compared to  $S = -0.0038$  for the as-cast film.

The fluorescence yield (FY) detection mode of NEXAFS analyzes fluorescence photons that are emitted as a result of an absorption process, and relative to PEY, it is more bulk sensitive, probing about 100 nm into the film.<sup>S7</sup> FY data was collected for pristine DTI and P3HT:DTI films. Similar to the PEY data, orientation analysis reveals that generally, the molecules become more edge-on with thermal annealing, as shown in Figure S10. The FY spectra show a much greater

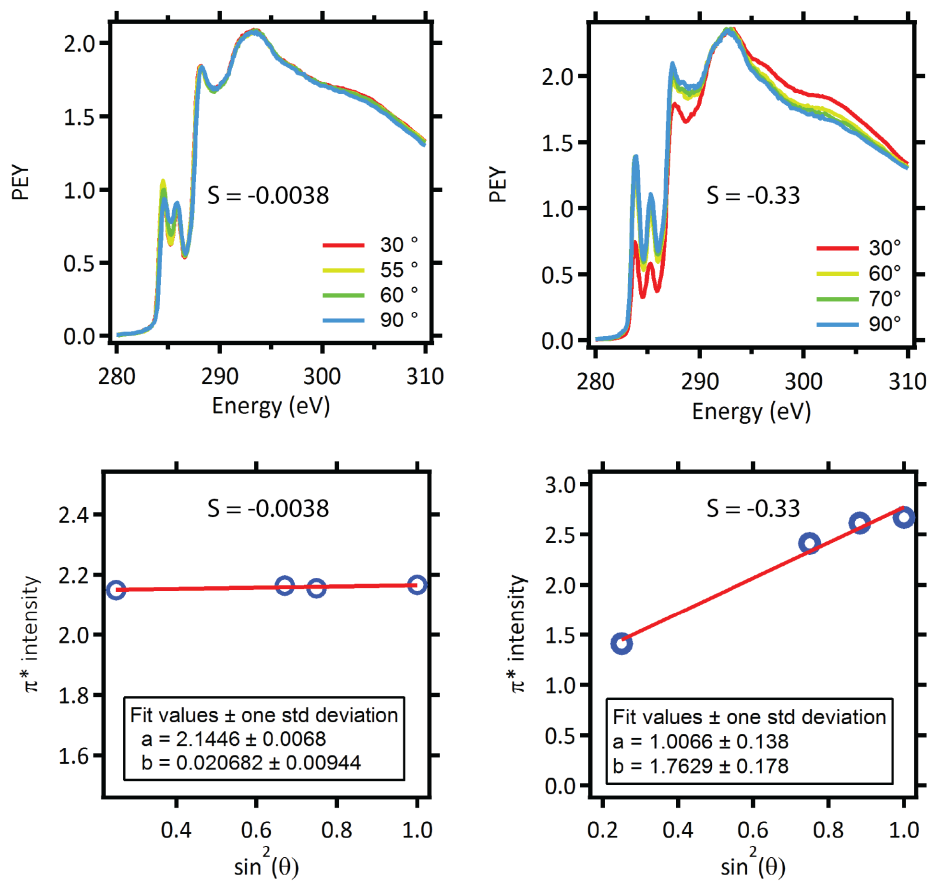


Figure S9: PEY carbon K edge spectra taken at different incident angles for a) an as-cast DTI film and c) an annealed DTI film. The area under the  $\pi^*$  peaks is plotted vs.  $\sin^2(\theta)$  and fit to a line for b) the as-cast film and d) the annealed film.

intensity of the  $\pi^*$  transitions relative to the higher energy  $\sigma^*$  transitions as compared to the PEY spectra. This is likely to occur because the alkyl chains of both DTI and P3HT populate the surface of the film to minimize surface energy. Since Auger emission is enhanced over fluorescent photon emission for carbon by over two orders of magnitude, the signal-to-noise ratio of the FY data is much less than the PEY data.<sup>S8</sup> Overall, the values of  $S$  are more negative for the annealed and blend films based on FY compared to PEY. It is possible that the molecules have more edge-on character in the bulk compared to the surface. However, the noisier FY data means that the linear fits of  $I_{\pi^*}$  vs.  $\sin^2(\theta)$  were not as good.

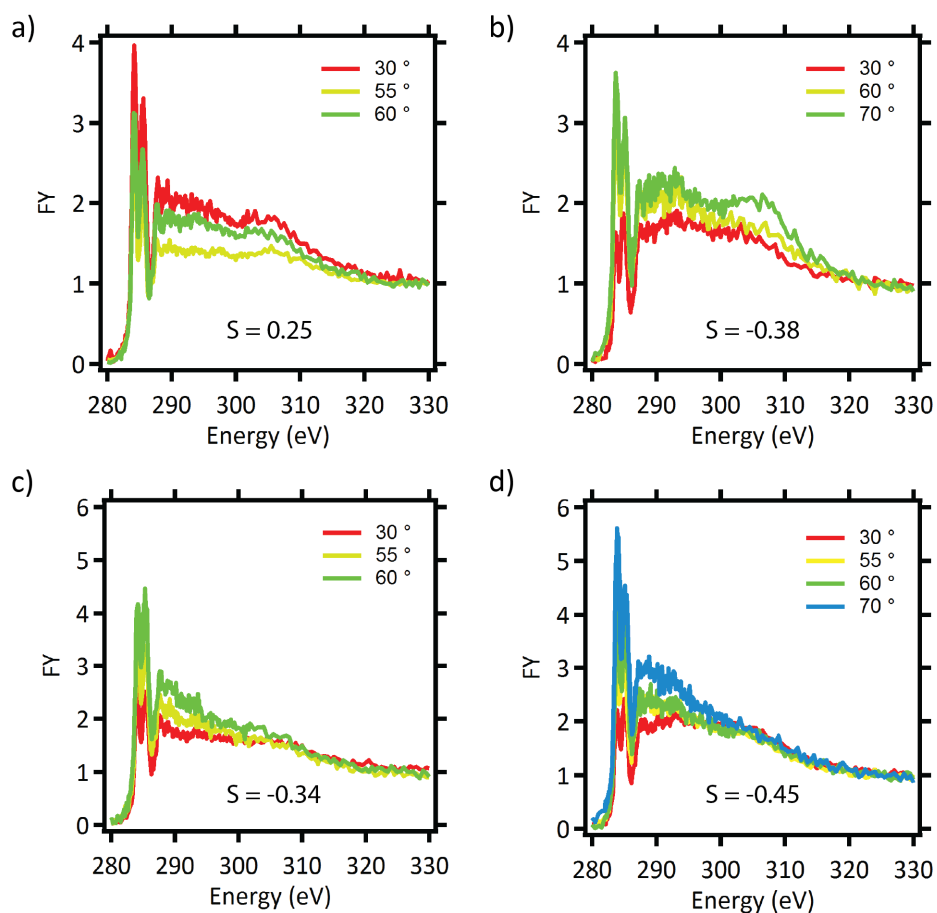


Figure S10: FY carbon K edge spectra taken at different incident angles for a) an as-cast DTI film, b) an annealed DTI film, c) an as-cast P3HT:DTI blend, and d) an annealed P3HT:DTI blend. The values of the orientation order parameter are indicated.

## Contribution from DTI to overall orientation of blend films

The orientation order parameter for as-cast and annealed blend films indicated a greater degree of edge-on character in the annealed blend. However, the  $\pi^*$  peak in the PEY data of the blends is a composite of the  $\pi^*$  peaks from DTI and P3HT. It is difficult to separate the contributions from P3HT and DTI since they overlap significantly. To get a sense of the relative contribution from DTI to the overall blend orientation in as-cast and annealed films, the composition, or % DTI, of the  $\pi^*$  peak in the blends was determined based on a linear combination of  $\pi^*$  peaks of the pure DTI and P3HT components. Highly edge-on molecules exhibit a large difference in total  $\pi^*$  intensity between incident angles of  $30^\circ$  and  $90^\circ$ , as seen in Figure S9 for annealed DTI. Therefore, if DTI is much more edge-on relative to P3HT in the annealed film compared to the as-cast film, then the increase in % DTI of the composite  $\pi^*$  peaks from  $30^\circ$  to  $90^\circ$  should be greater in the annealed film. Figure S11 shows the % DTI for different incident angles of the as-cast and annealed blends. It is clear that the annealed blend has an overall greater fraction of DTI and the increase in % DTI from  $30^\circ$  to  $90^\circ$  (35% to 55%) is greater than the as-cast blend (28% to 40%). This supports the claim that the thermally induced reorientation in the blends is mostly a result of changes in DTI.

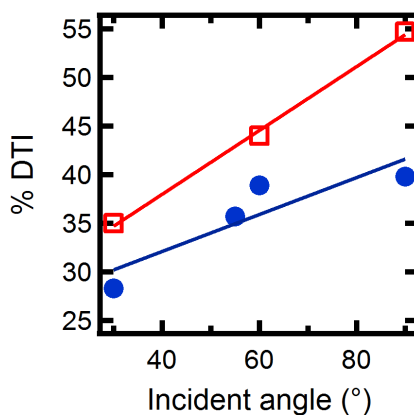


Figure S11: % DTI as a function of incident angle for as-cast (blue circles) and annealed (red open squares) P3HT:DTI blend films. The % DTI was determined based on a linear combination of the  $\pi^*$  peaks of the pure P3HT and DTI components. The lines represent linear fits to the data.

## Electron-only and hole-only diodes

Thermal annealing leads to a significant decrease in the electron current as expected based on the reorientation of the DTI molecules. However, since P3HT does not undergo the same type of reorientation, and possibly becomes more crystalline with annealing, the hole current is not expected to decrease significantly with annealing since holes travel predominantly through P3HT domains. Figure S12 shows the dark J-V behavior of as-cast and annealed electron-only and hole-only diodes. It is clear that annealing leads to a significant drop in the electron current, but not in the hole current. The experimental data was fit with a Mott-Gurney relation,  $J = \frac{9}{8} \mu \epsilon_0 \epsilon_r \frac{V^2}{L^3}$ , where  $\mu$  is the mobility,  $\epsilon_0$  is the permittivity of free space,  $\epsilon_r$  is the dielectric constant of the material, assumed to be 3.8, and  $L$  is the film thickness which was set to 100 nm. Using this relation, the electron and hole mobilities can be estimated. For the electron-only diode, the electron mobility decreased from  $\mu_e = 4.1 \times 10^{-6} \frac{\text{cm}^2}{\text{V} \cdot \text{s}}$  to  $\mu_e = 1.8 \times 10^{-7} \frac{\text{cm}^2}{\text{V} \cdot \text{s}}$  for the as-cast and annealed devices, respectively. Alternatively, the mobility in the hole-only devices did not change significantly, with a mobility of  $\mu_h = 3.7 \times 10^{-5} \frac{\text{cm}^2}{\text{V} \cdot \text{s}}$  and  $\mu_h = 6.9 \times 10^{-5} \frac{\text{cm}^2}{\text{V} \cdot \text{s}}$  for the as-cast and annealed devices, respectively.

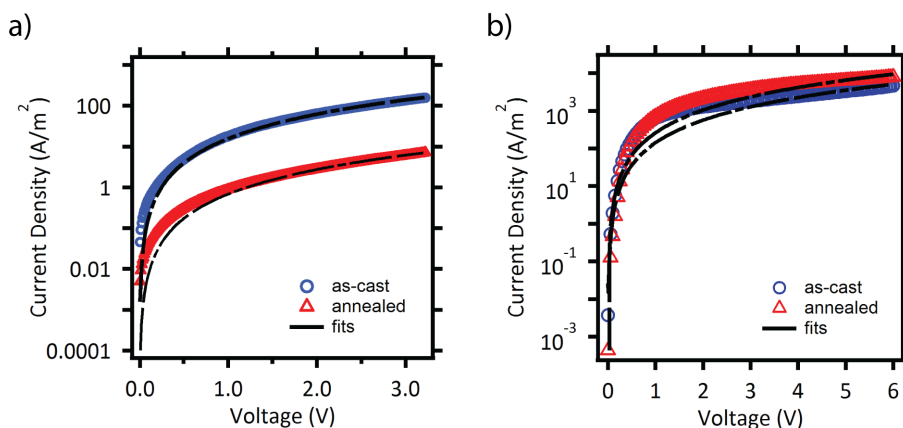


Figure S12: J-V curves taken in the dark for (a) an electron-only and (b) a hole-only diode. Device geometry for the electron-only diode was glass/Al/P3HT:DTI/Ca/Al, and glass/ITO/PEDOT:PSS/P3HT:DTI/Au for the hole-only diode. Data was fit with a Mott-Gurney relation.

## GIWAXS studies

### Hexagonal packing

The GIWAXS pattern of annealed DTI films shows a pattern indicative of hexagonal packing. The reciprocal space pattern of a hexagon is another hexagon that is rotated by  $30^\circ$ . Therefore, a hexagonal structure oriented with one of its flat sides parallel to the substrate would have a scattering pattern that includes a reflection nearly out-of-plane (close to the  $q_z$  axis), and another reflection at an angle  $60^\circ$  from the vertical axis. To visualize this, the 2D GIWAXS patterns can be plotted as  $q$  vs. polar angle. This is shown in Figure S13. It is clear that the spots of high intensity for the reflection at  $0.29 \text{ \AA}^{-1}$  are at polar angles near  $0^\circ$  and  $60^\circ$ , as expected for hexagonal packing.

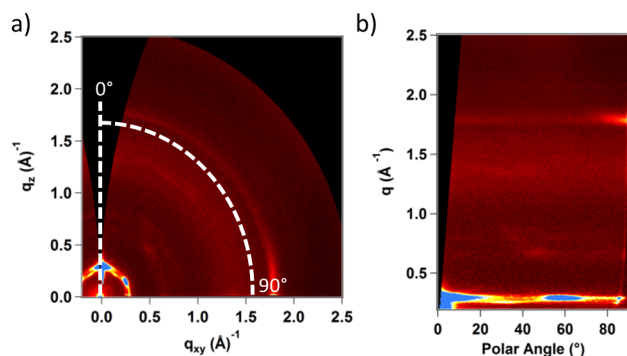


Figure S13: (a) A typical 2D GIWAXS pattern of an annealed pristine DTI film showing intensity as a function of the in-plane and out-of-plane components of the scattering wave vector. (b) This can be transformed to show  $q$  as a function of polar angle ( $^\circ$ ).

### *In situ* experiments

*In situ* GIWAXS experiments were done to examine the temperatures and time scales required for DTI reorientation. *In situ* experiments where the sample was incrementally heated, allowed to equilibrate, and then a scattering pattern taken were performed on the P3HT:DTI blend (Figure S14). Additionally, an isothermal experiment was performed where the sample was heated to  $120^\circ\text{C}$  and GIWAXS data taken over time. This is shown for a P3HT:DTI blend in Figure S15. Note that it does take several minutes for the sample to reach  $120^\circ\text{C}$  when heated from room

temperature. It is clear that in the time it takes the hot plate to reach 120 °C, the characteristic hexagonal pattern and in-plane  $\pi$ - $\pi$  stacking of annealed DTI is already apparent, and this pattern becomes more well defined with time.

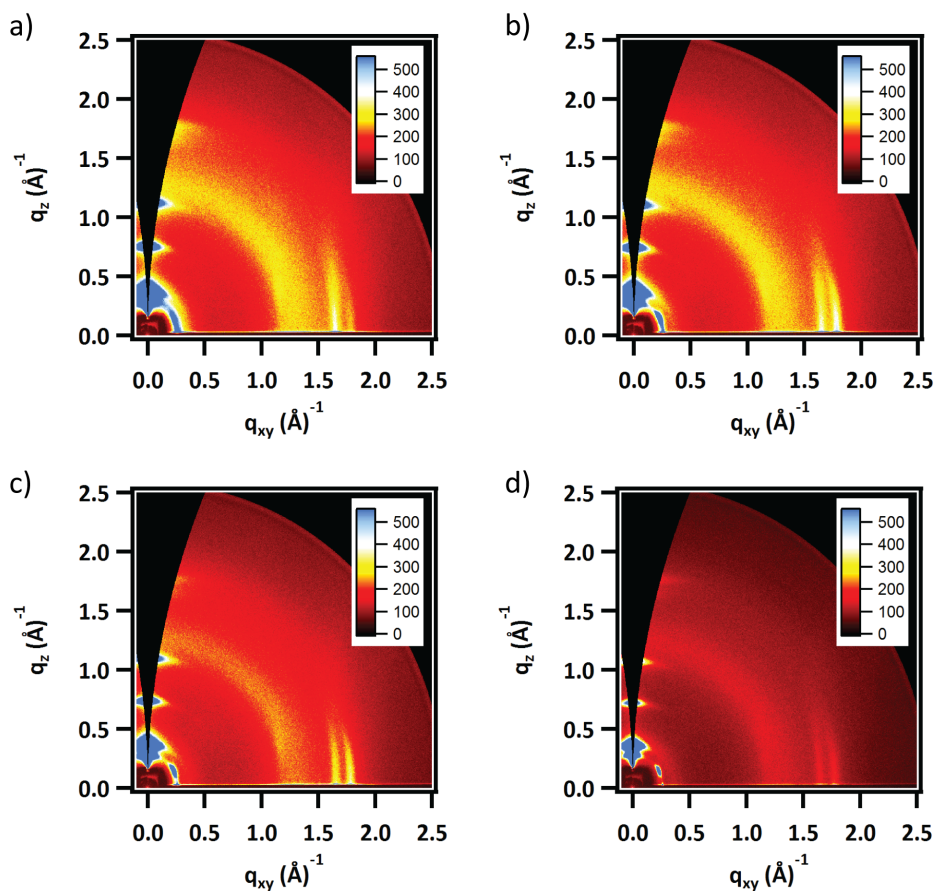


Figure S14: *In situ* GIWAXS patterns of a P3HT:DTI blend film taken during heating at a) 60 °C, b) 70 °C, c) 80 °C, and d) 120 °C.

Similar *in situ* GIWAXS studies, both at temperature during incremental heating and as a function of time at 120 °C, were done for pristine DTI films. *In situ* scattering at incremental temperatures reveals that, similar to the blend, the typical hexagonal pattern begins to form in the reflection at  $0.29 \text{ \AA}^{-1}$  even at 40 °C, as shown in Figure S16. This is close to the temperature where the exothermic peak on heating is observed in the DSC, suggesting again that this is a cold crystallization peak. Further heating leads to the pattern becoming more well-defined and the intensity of the  $\pi$ - $\pi$  stacking peak becomes more concentrated in-plane. When pristine DTI is heated to 120 °C and examined as a function of time (Figure S17), it is again observed that by the time

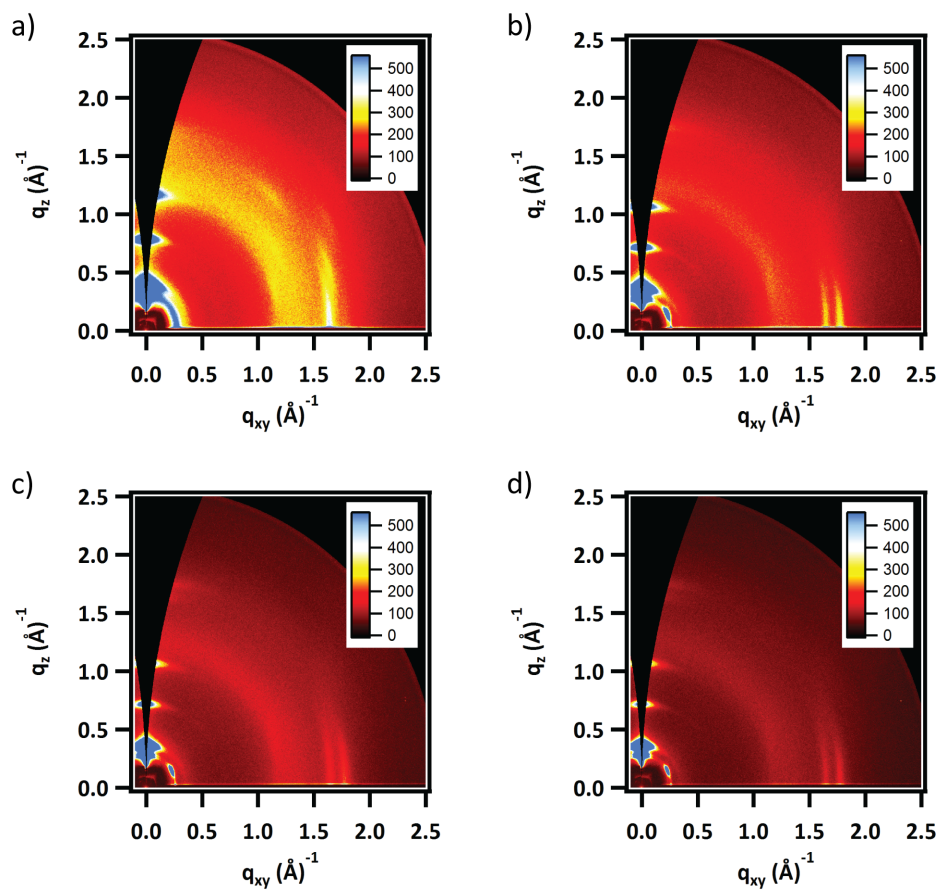


Figure S15: *In situ* GIWAXS patterns of a P3HT:DTI blend film at a) room temperature, b) once the sample reached 120 °C, c) 6 minutes after reaching 120 °C, and d) 20 minutes after reaching 120 °C.

the sample temperature reaches 120 °C, the hexagonal reflection at  $0.29 \text{ \AA}^{-1}$  and in-plane  $\pi$ - $\pi$  stacking is already observed. Again, this pattern becomes more defined with time. *In situ* data on the pristine DTI film is similar to the P3HT:DTI blend, however, it seems that the characteristic annealed scattering pattern evolves at lower temperatures and shorter annealing times. This is suggestive that blending P3HT and DTI somewhat inhibits the kinetics of reorientation and ordering of DTI.

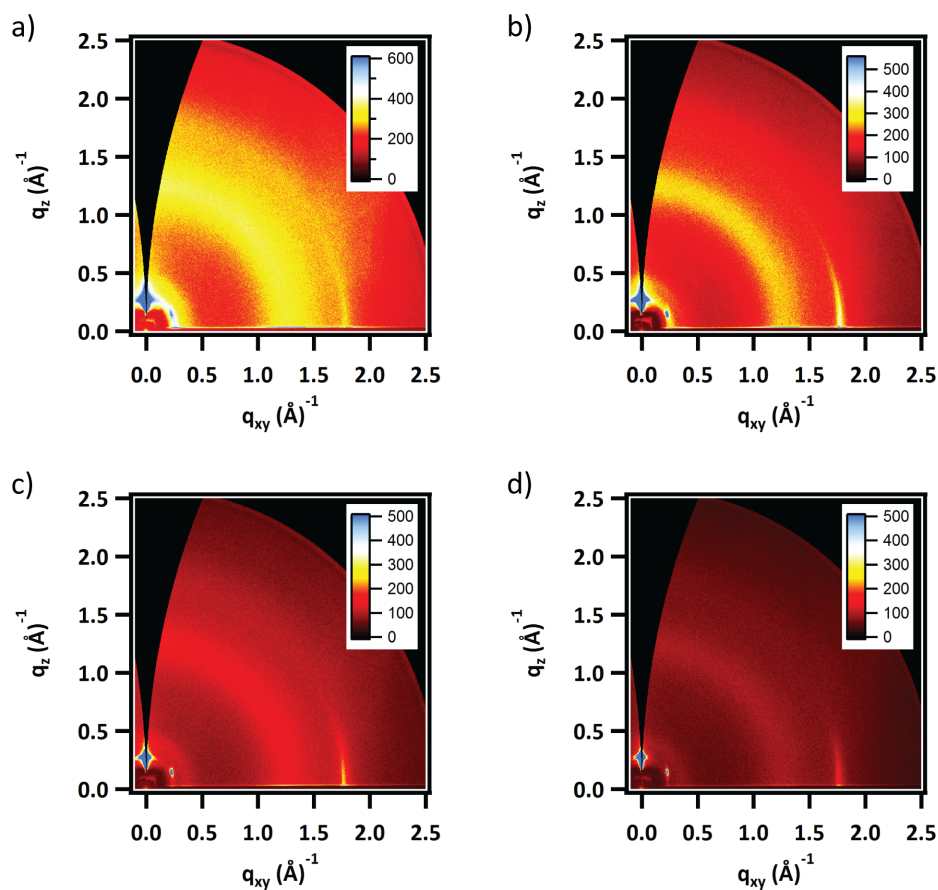


Figure S16: *In situ* GIWAXS patterns of a pristine DTI film taken during heating at a) 40 °C, b) 60 °C, c) 80 °C, and d) 120 °C.

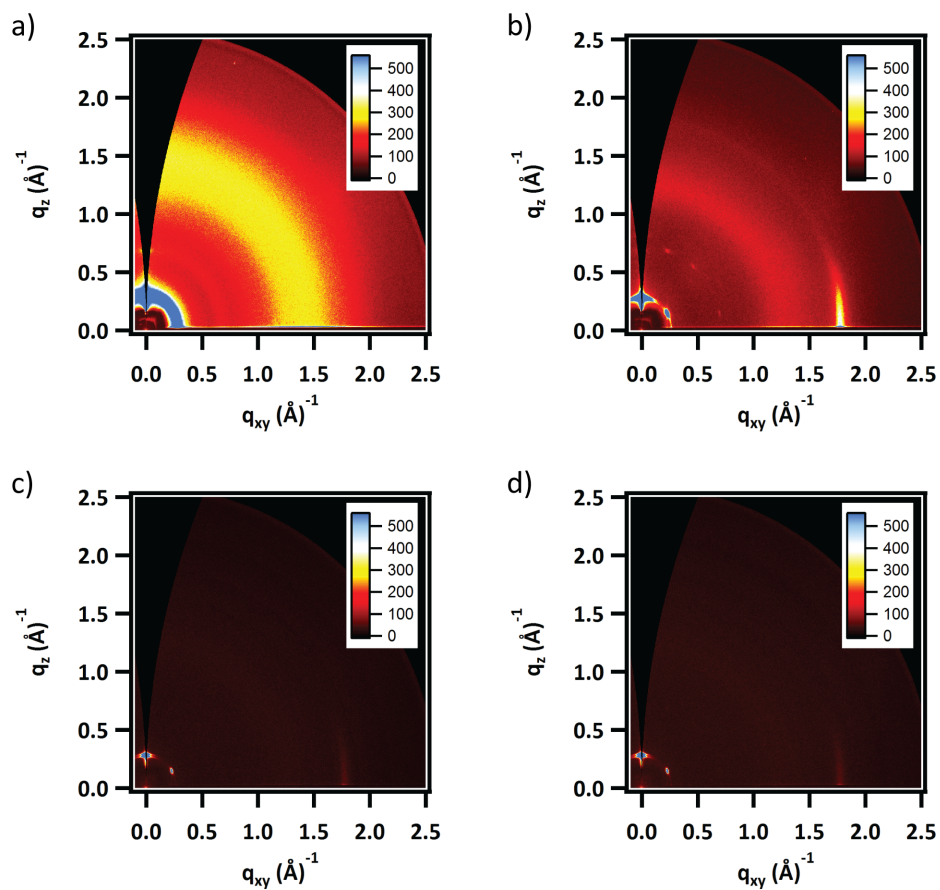


Figure S17: *In situ* GIWAXS patterns of a pristine DTI film at a) room temperature, b) once the sample reached 120 °C, c) 10.5 minutes after reaching 120 °C, and d) 20 minutes after reaching 120 °C.

## Correlation lengths

X-ray scattering experiments also provide a way to probe changes and development in crystallite correlation lengths that result from annealing. The width of diffraction peaks can provide information on correlation lengths within the sample and potentially grain or crystallite sizes. The simplest way to extract information on the coherence length,  $L_c$  is through the Scherrer equation,<sup>S9,S10</sup>

$$L_c = \frac{2\pi K}{\Delta_q},$$

where  $K$  is the shape factor (typically 0.8 - 1) and  $\Delta_q$  is the full width at half-maximum (FWHM) of a diffraction peak. However, care must be taken when using the Scherrer formula as it assumes that only crystalline size contributes to peak width, and ignores disorder. The results of Scherrer analysis should be considered more as correlation lengths between regions of disorder as opposed to true crystallite sizes. Nevertheless, this still provides a useful way to track changes in correlation lengths.

Peak width analysis was performed on as-cast and annealed (120 °C for 20 min) P3HT:DTI blends to estimate changes in correlation lengths and crystallite size. Scattering peaks were fit with either a Gaussian or Lorentzian line-shape in order to determine the peak position and FWHM. Fits were performed for scattering in the nearly out-of-plane direction (along  $q_z$ ) for the alkyl stacking extent of DTI (centered at  $\sim 0.29 \text{ \AA}^{-1}$ ) and the (100) reflection of P3HT (centered at  $\sim 0.38 \text{ \AA}^{-1}$ ). This provides information on the vertical height of stacked DTI aggregates and P3HT crystallites. Additionally, the extent of in-plane  $\pi$ - $\pi$  stacking was determined by fits along the in-plane portion (along  $q_{xy}$ ) of the  $\pi$ - $\pi$  stacking reflections. Representative fits are shown in Figure S18a and S18b. Changes in correlation lengths in the out-of-plane extent are shown in Figure S18c, and the in-plane  $\pi$ - $\pi$  extent in Figure S18d.

The most significant change in correlation length is for the out-of-plane alkyl stacking extent of DTI with thermal annealing. This suggests that annealing leads to aggregates of separate DTI columns that in total may be quite high, nearly 50 nm. On the contrary, the length of these DTI

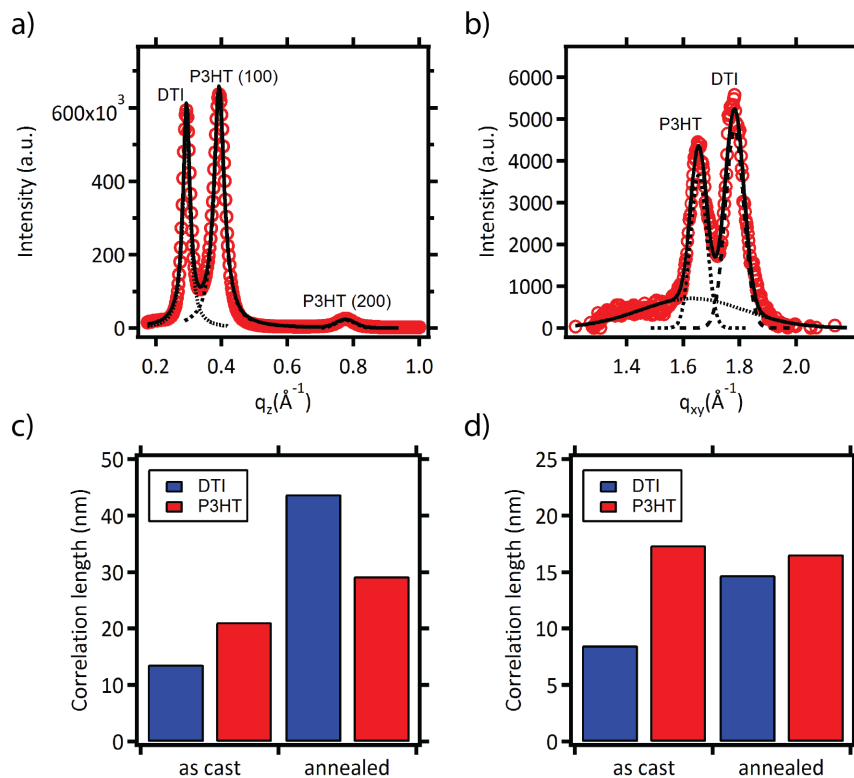


Figure S18: Representative example of peak fitting for (a) the nearly out-of-plane scattering and (b) in-plane scattering near the  $\pi$ - $\pi$  stacking distance for an annealed P3HT:DTI blend. Correlation lengths in the nearly out-of-plane direction determined from Scherrer analysis are shown in (c) for the hexagonal reflection of DTI and the (100) reflection of P3HT. (d) shows the in-plane  $\pi$ - $\pi$  stacking correlation lengths for DTI and P3HT.

columns does not seem to change much based on the width of the  $\pi$ - $\pi$  stacking peak, as it only varies from  $\sim 8$  nm to  $\sim 15$  nm for as-cast and annealed blends, respectively.

It is possible that charge transport through separate stacks of DTI molecules can occur even if their  $\pi$ - $\pi$  stacking directions are not perfectly parallel. Charges may still find pathways for transport in an as-cast film that consists of stacks of DTI with no preferential orientation. Peak width data suggests that annealing does not lead to a large increase in the lengths of DTI columns, so the reduced performance of annealed devices is likely mostly due to reorientation and stacking of separate DTI columns.

## Crystallite orientation

Crystallite orientation can be determined from 2D GIWAXS patterns based on the intensity distribution over polar angle ( $^\circ$ ) of a given reflection. Crystallites with no preferred orientation will appear as a ring of scattering in 2D scattering patterns. Figure S19 shows the intensity distribution as a function of polar angle for the (100) reflection of P3HT and the alkyl stacking reflection for DTI located at  $\sim 0.29 \text{ \AA}^{-1}$  as a function of temperature during annealing. It is clear that the intensity distribution of P3HT remains relatively constant with annealing, indicating there is little reorientation of P3HT crystallites. The characteristic hexagonal pattern of annealed DTI shows up very clearly by  $70 \text{ }^\circ\text{C}$ .

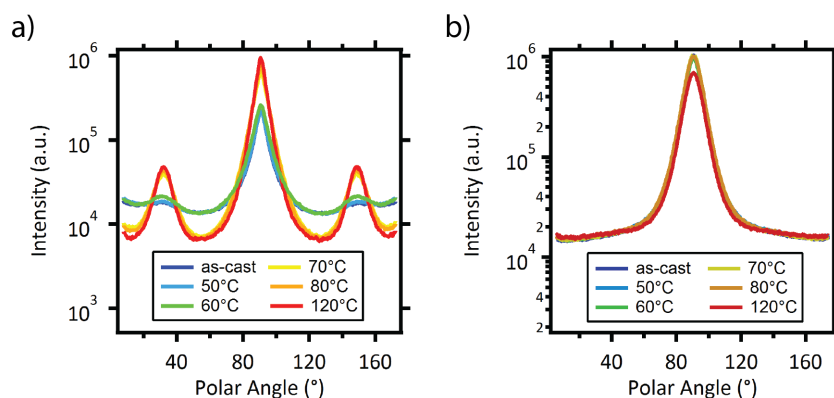


Figure S19: Intensity distribution as a function of polar angle ( $^\circ$ ) for (a) the alkyl stacking reflection of DTI and (b) the (100) reflection for P3HT taken at various temperatures during annealing.

## DSC

Additional DSC data on pristine DTI and pristine P3HT is shown in Figure S20a. Also, a closer look at the crystallization peak of P3HT during cooling (around 200 °C) reveals that when mixed with DTI, P3HT crystallizes at a lower temperature, as seen in Figure S20b. This suggests that DTI may also slightly inhibit the crystallization of P3HT.

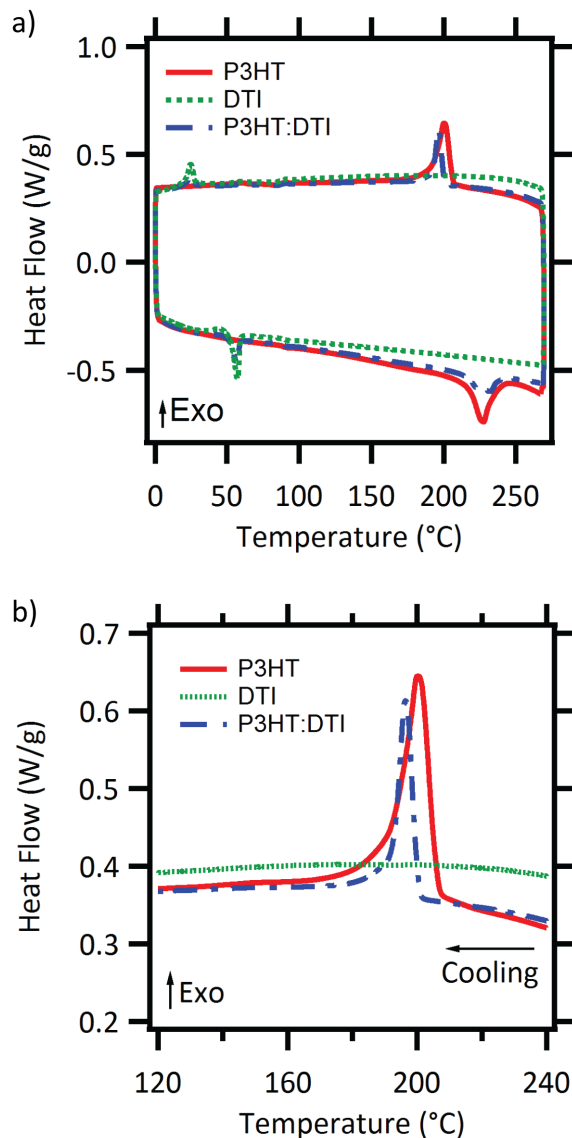


Figure S20: (a) DSC scans of pristine P3HT (red curve), pristine DTI (green dashed curve), and a 1:1 by mass P3HT:DTI blend (blue dotted-dashed curve). A zoom in of the crystallization peak of P3HT is shown in (b). The heating and cooling rate was 10 °C/min.

## References

- (S1) Pho, T. V.; Toma, F. M.; Chabynec, M. L.; Wudl, F. *Angewandte Chemie International Edition* **2013**, *52*, 1446–1451.
- (S2) Gann, E.; Young, A. T.; Collins, B. A.; Yan, H.; Nasiatka, J.; Padmore, H. A.; Ade, H.; Hexemer, A.; Wang, C. *Review of Scientific Instruments* **2012**, *83*, 045110.
- (S3) Cisse, L.; Destruel, P.; Archambeau, S.; Seguy, I.; Jolinat, P.; Bock, H.; Grelet, E. *Chemical Physics Letters* **2009**, *476*, 89 – 91.
- (S4) Mach, P.; Pindak, R.; Levelut, A.-M.; Barois, P.; Nguyen, H. T.; Baltes, H.; Hird, M.; Toyne, K.; Seed, A.; Goodby, J. W.; Huang, C. C.; Furenlid, L. *Phys. Rev. E* **1999**, *60*, 6793–6802.
- (S5) Mezger, M.; Jérôme, B.; Kortright, J. B.; Valvidares, M.; Gullikson, E. M.; Giglia, A.; Mahne, N.; Nannarone, S. *Phys. Rev. B* **2011**, *83*, 155406.
- (S6) Genzer, J.; Kramer, E. J.; Fischer, D. A. *Journal of Applied Physics* **2002**, *92*, 7070–7079.
- (S7) Hähner, G. *Chemical Society Reviews* **2006**, *35*, 1244–1255.
- (S8) Bao, Z.; Locklin, J. *Organic Field-Effect Transistors*; CRC Press, 2007.
- (S9) Scherrer, P. *Gottinger Nachrichten Math. Phys* **1918**, *2*, 98–100.
- (S10) Smilgies, D.-M. *Journal of Applied Crystallography* **2009**, *42*, 1030–1034.